

Plasmonic Nanostructure Design for Efficient Light Coupling into Solar Cells

Vivian E. Ferry, Luke A. Sweatlock,[†] Domenico Pacifici, and Harry A. Atwater*

Thomas J. Watson Laboratories of Applied Physics, California Institute of Technology, Pasadena, California 91125

Received July 25, 2008; Revised Manuscript Received October 29, 2008

ABSTRACT

We demonstrate that subwavelength scatterers can couple sunlight into guided modes in thin film Si and GaAs plasmonic solar cells whose back interface is coated with a corrugated metal film. Using numerical simulations, we find that incoupling of sunlight is remarkably insensitive to incident angle, and that the spectral features of the coupling efficiency originate from several different resonant phenomena. The incoupling cross section can be spectrally tuned and enhanced through modification of the scatterer shape, semiconductor film thickness, and materials choice. We demonstrate that, for example, a single 100 nm wide groove under a 200 nm Si thin film can enhance absorption by a factor of 2.5 over a 10 μm area for the portion of the solar spectrum near the Si band gap. These findings show promise for the design of ultrathin solar cells that exhibit enhanced absorption.

Photovoltaics (PV) technology is currently enjoying substantial growth and investment. Although there are many approaches to photovoltaic cell design and fabrication, the key performance metric is the cost per watt of PV-generated electricity, which motivates a reduction in material utilization facilitated by enhanced optical absorption. To date, little systematic thought has been given to the question of how plasmon excitation and light localization might be exploited to advantage in photovoltaics. Using insights derived from the other phenomena studied in the plasmonics field, we outline approaches to dramatically modify the light absorption in thin film solar cells. In particular, the ability of plasmonic structures to localize light at subwavelength dimensions is synergistic with use of ultrathin thin film absorbers, as well as quantum well, quantum dot, and potentially molecular photovoltaic absorber materials.

Conventionally, it is thought that photovoltaic absorbers must be optically "thick" to enable nearly complete light absorption and photocarrier current collection. Typically these absorbers are semiconductors with thicknesses several times the optical absorption length; for silicon this thickness is greater than 100 μm , and it is several micrometers for direct bandgap compound semiconductors. Furthermore, high-efficiency cells must have minority carrier diffusion lengths several times the material thickness. Thus solar cell design and material synthesis considerations are strongly dictated by this simple optical thickness requirement.

On the other hand, thin film solar cells show promise as economic alternatives to conventional silicon-wafer-based photovoltaics, combining high efficiency with low processing and materials costs,¹ and thin film cells of CdTe,² amorphous Si,³ and CuIn_xGa_{1-x}Se₂^{4,5} (CIGS) have been fabricated with absorbing layers a few micrometers thick. Reducing the cell thickness can increase the conversion efficiency, since the dark current resulting from bulk recombination decreases with decreasing thickness. Thin absorber layers could also significantly expand the range and quality of absorber materials that are suitable for photovoltaic devices by enabling efficient photocarrier collection across short distances. This allows for the use of low-dimensional structures such as quantum dots and wells, of inexpensive materials such as polycrystalline thin semiconductor films with low minority carrier diffusion lengths, and of novel materials with advantageous optical properties but poor electronic performance, such as polymers. So long as the layer can be made to absorb a significant fraction of the incident light, there is potential not only for cost and weight reduction with thinned layers but also for conversion efficiency enhancement associated with an increased carrier excitation level in the cell.

In conventional cell designs, efficiencies of nanometer-thickness cells are strongly limited by decreased absorption, carrier excitation, and photocurrent generation, and so new strategies for enhanced absorption and light trapping are desirable.^{6,7} Conventional light trapping schemes use wavelength-scale surface texturing on the front or back of the cell to enhance light absorption. These features, often several micrometers high, are too large to be used with extremely

* Corresponding author.

[†] Current address: Space Technology Research Laboratories, Northrop Grumman Space Technology, Redondo Beach, CA 90278.

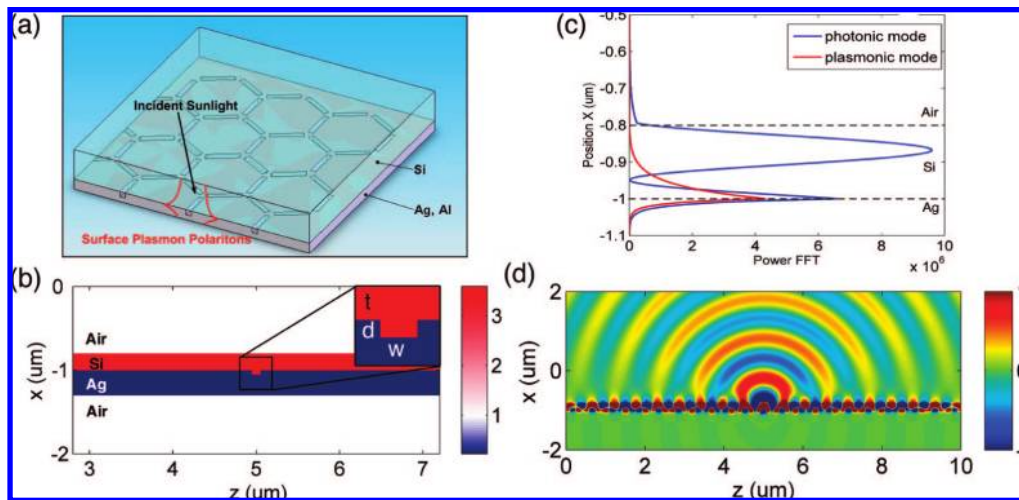


Figure 1. Simulation of scattered H_y field at $\lambda = 1000$ nm in 200 nm Si film on 300 nm of Ag. Metallic nanostructured scattering objects are on the Si/Ag interface ($x = -1$). (a) A 3D conceptual schematic of a solar cell with subwavelength grooves tiled on a back Ag contact. (b) The schematic outline of the device layer in the simulation, with the inset of panel b defining the width and depth of a groove. (c) The modal profiles of the two identified modes, plotting power as a function of position in the waveguide. (d) The H_y scattered field off of a 100 nm wide by 50 nm deep groove filled with Si. Several waveguide modes are present.

thin films, since the total film thickness is smaller than the surface roughness.⁸

Metallic nanostructured thin films, which support surface plasmon polaritons (SPPs), have the potential to confine and guide incident sunlight into wavelength-scale or subwavelength thickness absorber layer volumes.⁹ SPPs are collective oscillations of free electrons at the boundary of a metal and a nonconducting dielectric or semiconductor material.^{10–12} These modes are highly localized at the metal surface and can propagate for several micrometers with minimal loss, but the metal film must be nanostructured because the momentum mismatch between photons propagating in dielectric media and SPPs prohibits their direct excitation by incident light. Coupling to SPPs results in absorption in a mode volume that is small relative to the exponential absorption profiles that occur in conventional bulk semiconductors.¹³ Enhanced absorption thus increases the solar cell's photocarrier injection level and has the potential to achieve performance resembling that of a concentrator cell in which increasing the carrier injection level increases the open circuit voltage.

Previous studies incorporating surface plasmons in photovoltaics have mainly focused on the large resonant scattering cross sections of plasmonic nanoparticle structures fabricated on the top surface of a thin semiconductor film with no back contact.^{14–16} This paper investigates a different geometry of plasmonic solar cell, shown conceptually in the three-dimensional (3D) schematic of Figure 1a, consisting of a thin semiconductor absorber film with an underlying nanostructured plasmonic waveguide as the back contact. The nanostructures in this case are subwavelength grooves, tiled to be polarization independent. The incident light is scattered at the metal–semiconductor interface by a subwavelength object into propagating modes in the metal–semiconductor interface plane, transverse to the incident light direction. The energy in propagating modes, including SPPs, can be partially absorbed by the semiconductor layer, although some

will be dissipated via Ohmic losses in the metal. This geometry decouples the direction of optical absorption, which is in-plane, from the direction of carrier collection, which is out-of-plane. Our group has previously experimentally demonstrated bulklike absorption in a monolayer-thick CdSe quantum dot film, which has inspired our further design and optimization of the incoupling structures.¹³ We mainly focus on Si here, as it is the most prevalent, abundant, and well-established photovoltaic absorbing material, as well as being the material system considered in other plasmonic solar cell designs,^{14,15} but the design rules enumerated here are easily extended to a wide range of materials. In the last section, we compare the absorption enhancements in Si and GaAs thin films and discuss the consequences of different choices for the backside metal.

Historically, optical excitation of SPPs has been performed by prism coupling,^{17,18} and more recently by gratings,¹⁹ which can be highly efficient but limited in both wavelength and angular range. The diffraction and scattering of small apertures have been studied for a number of years,^{20,21} with particular attention recently to the transmission properties of holes and slits.^{22–28} We have recently found that as few as four scatterers are sufficient to fabricate efficient gratings based on subwavelength slits.²⁸ Gratings with small numbers of elements are interesting because they are less frequency selective, and we show here that the limiting case of a single scattering object, such as a ridge or a groove in a metallic film, can also act as a relatively efficient broadband coupler from freely propagating modes to guided modes.^{13,29,30} Although efficient and practical incoupling structures will employ periodic or aperiodic arrays of scattering objects, our focus in this paper is on single scattering objects so as to discern the scattering physics by itself. A future paper will address design of arrays of scatterers.

We use quantitative full-field electromagnetic simulation that employs the finite-difference time domain (FDTD) method to assess the incoupling cross section σ of various

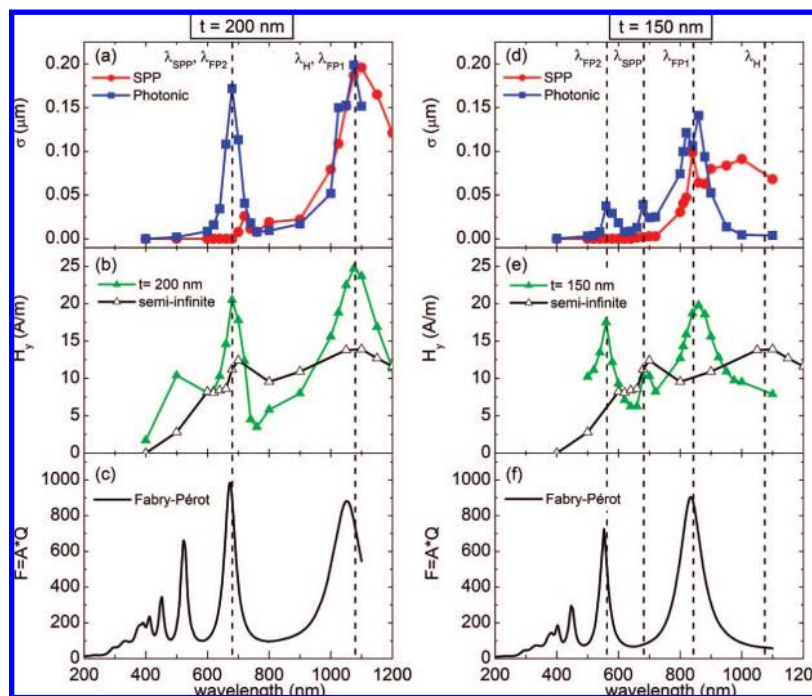


Figure 2. Calculated incoupling cross sections (σ), H_y field magnitudes, and quality factor for the Fabry-Pérot cavity in the Si film: left column for 200 nm thick film of Si, right column for 150 nm thick film of Si, both on Ag with a 100 nm wide by 50 nm deep groove cut into the Ag at the interface. Panels a and d show the incoupling cross sections for each mode across the spectral range where Si shows significant response. Panels b and e show the H_y field magnitude measured at the center of the groove mouth for each slab (green) and a semi-infinite layer of Si on Ag (black line). Panels c and f show the factor $F = A \cdot Q$, where A is the absorbance in the thin film and Q is the quality factor for a cavity of thickness t on Ag, without a groove.

incoupling structures across the solar spectrum and to determine the angular dependence of the absorption enhancement effects. Figure 1b shows the schematic of a typical structure we simulated, a 200 nm thick layer of Si on 300 nm of Ag with a single 100 nm wide by 50 nm deep groove etched into the Ag. Each simulation generates a map of time-harmonic electromagnetic fields for a steady-state plasmonic device with continuous wave, monochromatic input. Figure 1d shows the H_y field of the structure illustrated in Figure 1b. Depending on the thickness of the absorbing material, additional waveguide modes may be present; we call these modes photonic modes since they more closely resemble the slab waveguide modes of finite thickness planar dielectric films. The photonic and SPP modes differ in their spatial overlap with the semiconductor and metal layers and, hence, in the ratio of enhancement of semiconductor photoabsorption to metallic Ohmic loss, but if properly designed both can contribute to photogeneration of charge carriers.

We developed an approach that allows for the modal decomposition of scattered light into the SPP and photonic modal components, using a postprocessing method of Fourier mode spectral analysis (FMSA) to calculate the spectrum of the guided modes. We separately consider the relative absorption fractions in the semiconductor and metal for various materials combinations. This technique allows us both to analyze features of each mode, such as the spatial energy density profile and the propagation lengths in the waveguide, and to connect to other design figures of merit such as the incoupling efficiency for a variety of scattering objects. For the structure represented in Figure 1a, only two

modes exist, and Figure 1c shows the modal profile for the two modes in the waveguide, plotting the power in each mode as a function of position in the waveguide. This allows us to visualize each mode more clearly: the SPP mode is bound to the Si/Ag interface, with power decaying exponentially into the waveguide, and the photonic mode is localized mainly in the Si slab.

The incoupling cross sections give a measure of the “effective size” of the scatterer for coupling light into specific modes, either plasmonic or photonic in nature. Since the simulations are 2D, the incoupling cross sections reported have units of length rather than area. Furthermore, the incoupling cross section gives an inkling of design parameters for arrays of light harvesting incouplers—for a single wavelength the scattering objects should be spaced σ apart to harvest all of the incident light. The details of the FMSA method and the calculation of the incoupling cross sections are shown in the Supporting Information. Although this paper addresses the design considerations for photovoltaic devices, the FMSA analysis method is general and is applicable to other devices, such as photodetectors or light sources.

Since we are interested in the broadband incoupling response for various nanostructures, we tested each scattering object across a range of incident wavelengths matching the region of the solar spectrum where silicon exhibits significant spectral response, from 400 to 1200 nm. Panels a and d of Figure 2 show typical examples of the incoupling cross sections for SPP modes and photonic modes in a device with a 100 nm wide by 50 nm deep groove cut into the Si/Ag interface. Figure 2a is for a device with a 200 nm thick Si

layer, and Figure 2d is for a 150 nm thick layer; all other conditions are identical. Both devices exhibit several strong peaks in σ , with σ generally increasing with increasing wavelength, where less energy is absorbed in the silicon slab before reaching the scatterer.

The modal incoupling efficiencies of these structures across the investigated spectral range can be described by the convolution of three different physical resonances in the device. First, the interference within the thin film leads to a resonant Fabry–Pérot cavity effect within the film at various wavelengths, depending on the film thickness.³¹ The multiple reflections at resonant frequencies in the film leads to stronger interaction of incident light with the scattering object and to increased incoupling into propagating modes. Second, at the SPP resonance frequency the high local fields near the scatterer lead to increased incoupling into the photonic waveguide modes. At this frequency the SPP has low group velocity and therefore is bound to the vicinity of the scattering object. Third, the incident light induces a polarization in the scattering object. For objects much smaller than the incident wavelength, the induced polarization is resonant at modes whose number and strength vary with the scatterer’s shape and dimensions.^{32,33} At these resonant frequencies the local fields near the scattering center are very high, and both the absorption cross section and the scattering cross section of the object will be at maximum. The incoupling ability over the entire spectral range is a combination of these three physical phenomena, and the frequency response of incoupling cross sections can be tuned by appropriate modifications of the layer thicknesses and scatterer geometries.

At all of these resonant conditions the field magnitudes will be high near the scattering object. Consequently the incoupling cross sections are large near resonant frequencies. In panels b and e of Figure 2, we calculate the field magnitudes at the centerpoint of the groove mouth for both finite thickness films and a semi-infinite film of Si, in order to separate thin film interference effects leading to resonances from inherent resonant properties of the groove. We see that the calculated incoupling cross sections show peaks that line up with the field magnitudes for the finite thickness slabs, from which we deduce that the field magnitude at the groove is a good indicator of incoupling efficiency.

To further investigate the effects of the film thickness on incoupling efficiency, we consider the interference in the thin film. The film can be modeled as a Fabry–Pérot cavity, where the two mirrors are the Si/Air and Si/Ag interfaces, characterized by reflectivities R_1 and R_2 , respectively. To quantify the absorption enhancements occurring at resonant cavity modes, we define a figure of merit $F = AQ$, where A is the thin film absorbance, i.e., the fraction of incident energy that gets absorbed in the film as a result of multiple reflections, and R and T are the thin film reflectance and transmittance.

$$A(\lambda) = 1 - R(\lambda) - T(\lambda)$$

Q is the approximate quality factor of a Fabry–Pérot cavity with thickness t , refractive index n , absorption coefficient α , and reflectivities R_1 and R_2 at the two interfaces, given by the following expression:

$$Q = 4\pi \frac{tn}{\lambda[1 - \exp(-2\alpha t)](1 - R_1)(1 - R_2)}$$

$[1 - \exp(-2\alpha t)]$ is the fraction of energy absorbed in the material in a cavity round trip, and the $1 - R_i$ factors account for the fractions of energy lost at reflection off each boundary. We calculate R_1 and R_2 from $R_i = |r_i|^2$, where r_i is the Fresnel reflection coefficient.³¹

The first peak in Figure 2a, at $\lambda = 680$ nm, is present in σ_{photonic} but is absent in σ_{SPP} . From comparison with Figure 2b and Figure 2c, we see that this point lines up with a maximum in the H_y field in both the slab and the semi-infinite film, as well as with one of the resonant frequencies of the 200 nm thick Si slab. We identify this peak as a product of both the SPP resonance and the Fabry–Pérot resonance of the film. If it were the Fabry–Pérot resonance of the film alone, the semi-infinite thickness slab would not have a field maximum at that frequency. This effect results in higher incoupling for the photonic mode, as the SPP mode is localized near its resonant frequency and its incoupling cross section is small in this range. For the 150 nm thick film, the Fabry–Pérot calculation of the film shows that there is no resonance at 680 nm, and so this is an appropriate case to deconvolve the two effects. We now see two peaks in both σ_{photonic} and $H_{y,150\text{nm}}$, at 580 nm (lining up with the blue-shifted Fabry–Pérot resonance due to the smaller film thickness) and at 680 nm, the SPP resonance. The semi-infinite film shows no field intensity peak at 580 nm, indicating that this incoupling peak is due to the Fabry–Pérot resonance alone. This incoupling maximum is observable only in the photonic mode, since the SPP mode has short propagation lengths at this frequency. A second Fabry–Pérot mode is observed at 840 nm, where again the $H_{y, \text{semi-infinite}}$ field is relatively low. Although not shown, we also compared the E_x and E_z field magnitudes across the spectrum, and at the Fabry–Pérot resonant frequencies the in-plane electric field also has a maximum, while the out-of-plane electric field is relatively constant. This is consistent with an out-of-plane resonant Fabry–Pérot mode in the slab.

The peak around 1100 nm observed for both film thicknesses is attributed to the magnetic dipole resonance of the groove. The semi-infinite structure, which is exempt from any Fabry–Pérot interference effects, shows a peak at 1100 nm, indicating that the enhanced incoupling is not due to the Q of the film. In the 200 nm thick film, there is significant scattering into both modes, and the position lines up with an additional Fabry–Pérot cavity mode, and so we attribute the peak to the convolution of the magnetic dipole with a Fabry–Pérot mode in the Si film. In the 150 nm thick film the effect is mainly on the SPP mode; for this reduced thickness, the photonic mode approaches its cutoff frequency.

We further investigate the nature of this maximum in incoupling cross section at 1100 nm by changing the width of the groove from 50 to 300 nm at fixed depth for the $t = 200$ nm case. Figure 3a shows the incoupling cross section σ , the “effective” width of the structure, against the physical size of the groove w . For the photonic mode, the incoupling cross section increases linearly with size, until it reaches 200 nm at which point it flattens out. For small grooves the

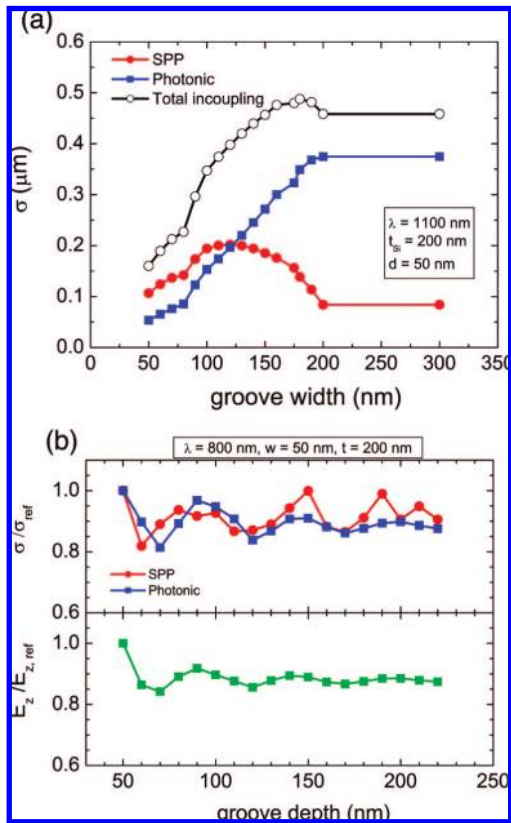


Figure 3. (a) Incoupling cross sections for a 50 nm deep groove with varying physical width w , at $\lambda = 1100$ nm. (b) Incoupling cross sections and field magnitudes for 50 nm wide groove with varying depth, at $\lambda = 800$ nm. The top panel shows the photonic and SPP incoupling cross sections, normalized to a reference groove that is 50 nm wide and 50 nm deep; the bottom panel shows the magnitude of the E_z field, measured at the centerpoint of the groove mouth, and normalized to the E_z field for the reference groove.

effective scattering cross section is proportional to the physical width w with ratio $\sigma = aw$. This relationship breaks down for larger grooves, which behave less like quasi-static dipole scatterers. Above $w = 200$ nm the edges of the groove act independently, and there is no further gain from increasing size. The incoupling to SPP modes is strongly affected by this dipole character; the SPP cross section peaks at $w = 110$ nm then declines for larger grooves. Since the number of photonic modes depends on the thickness of the absorbing layer, and for very thin devices only the plasmonic mode will be supported, this confirms that subwavelength scatterers are important for the thinnest devices.

Turning our attention from groovelike couplers to ridgelike couplers of the same aspect ratio, the scattering response changes, shown in Figure 4. Although the qualitative spectral shape is similar, with a peak at 680 nm and at 1100 nm, the incoupling cross sections are much higher for the ridge, and energy is predominantly coupled into photonic modes. For example, at $\lambda = 1100$ nm, the total incoupling cross section is $\sigma_{\text{groove}} = 0.35 \mu\text{m}$, with $\sigma_{\text{photonic}} = 0.15 \mu\text{m}$, while for the ridge the total incoupling cross section is $\sigma_{\text{ridge}} = 0.52 \mu\text{m}$, with $\sigma_{\text{photonic}} = 0.5 \mu\text{m}$. Intuitively this is reasonable because the ridge is a polarizable dipole-like scatterer located closer to the middle of the waveguide, whereas the groove is a

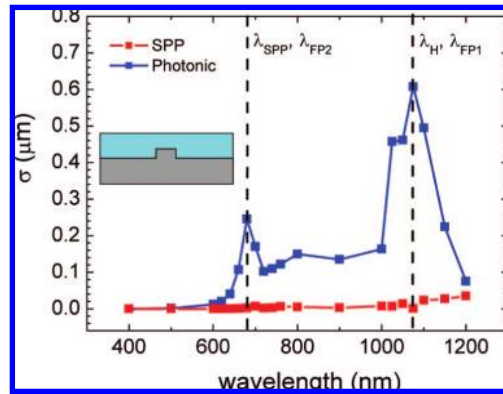


Figure 4. Incoupling cross sections for a 100 nm wide by 50 nm tall ridge of Ag in 200 nm of Si.

dipole-like scatter located in the plane of the metal–semiconductor interface. Although the total incoupling cross section is higher for the ridge, ultrathin devices that do not support photonic modes will be more efficiently served by subwavelength grooves.

Another type of resonance that could affect the incoupling efficiency of the groove is Fabry–Pérot cavity modes inside the groove itself. We probe the effect of this type of resonance by choosing a small width ($w = 50$ nm) and varying the depth incrementally from 50 to 220 nm at one incident wavelength ($\lambda = 800$ nm). In Figure 3b we show the ratio of the incoupling cross sections with respect to a reference groove that is 50 nm wide and 50 nm deep; the bottom panel shows the ratio of the magnitude of the E_z field at the groove mouth with respect to this same reference groove. The first interesting detail is that the shallowest groove studied, $d = 50$ nm, is the most efficient incoupler. As the groove gets deeper, the amplitude of the oscillation decreases, as more energy is absorbed within the groove and the field magnitude is weak at the interface. Most importantly, however, the variation with depth is quite small, and we conclude that while the Fabry–Pérot mode in the groove cavity is present, it is not a critical feature of design.

At this point we have found determining factors for the spectral shape of the incoupling cross sections, but we have not considered whether the energy in each mode is absorbed in the semiconductor or lost to the metal. Light coupled into a propagating mode can be absorbed in either material, but cell efficiency will only be improved when the absorption occurs in the semiconductor, which will be responsible for enhanced carrier generation in the cell. To this end, we use a separate computational method to calculate the absorption fractions in each material. Our spectral filtering method also allows us to determine power absorption in the semiconductor due to standard thin film reflection/transmission processes without the influence of the scattering. The average time–harmonic electromagnetic power absorbed in a given material depends on the divergence of the Poynting vector, $u_a = \nabla \cdot \mathcal{S}$.³⁴

$$u_a = \frac{1}{2} \int \omega \epsilon'' |\mathbf{E}|^2 + \omega \mu'' |\mathbf{H}|^2 dx dz$$

where ω is the frequency of the input wave, ϵ'' and μ'' are the imaginary parts of the permittivity and permeability, respectively, for the materials in the device, and $|\mathbf{E}|^2$ and $|\mathbf{H}|^2$ are the magnitudes of the electric and magnetic fields. In our structure, $\mu'' = 0$ for all our materials, and this second term drops out.

For each mode that propagates in the device, some portion of the energy will be absorbed in the semiconductor and some lost to the metal. There may also be localized resonances near the groove that are not coupled into propagating modes but still lead to local enhanced absorption. Although certain frequencies have much higher incoupling cross sections than others, the scattering efficiency shows relatively broad spectral features, and there may be significant absorption enhancement at nonresonant frequencies as well. These enhancements are for optical absorption only and do not necessarily correspond to actual generation of carriers. This calculation focuses only on the photon absorption by the material without accounting for the carrier generation and collection efficiencies.

The exact fractions of useful absorption to loss will of course depend on the wavelength and also on the choice of both semiconductor and metal. We define a figure of merit for absorption enhancement, the ratio of absorption in the semiconductor with a groove, u_a , to the absorption in an identical film without a groove, $u_{a,0}$. This will cancel out absorption enhancements due purely to the Fabry–Pérot resonances of the film but will preserve the effects of the groove and the propagating modes.

Figure 5 shows this absorption enhancement ratio for different materials combinations, in particular for Si (Figure 5a) and GaAs (Figure 5b). The absorption enhancements are calculated for the entire simulation volume, a $10 \mu\text{m} \times t$ area, with t the film thickness, and the groove at the center, which is equivalent to modeling an infinite linear array of scatterers, assuming a $10 \mu\text{m}$ spacing between elements. The incident beam is a $1 \mu\text{m}$ half-width Gaussian beam.

Looking at Figure 5 in more detail, we see that, with the exception of a few data points in the 200 nm of GaAs, the absorption enhancement ratio is always greater than 1. This demonstrates that the groove has significant broadband response and is not only effective at the resonant frequencies. The dips in both the Si and GaAs profiles correspond to the wavelengths with significant Fabry–Pérot resonance. In general, we see the strongest absorption enhancement for optically thin layers. Relatively opaque layers such as the 200 nm of GaAs will absorb a significant fraction of the light before it scatters and will have minimal interaction with the scattering center.

For the 200 nm thick layer of silicon in Figure 5a, the incoupling generally increases with increasing wavelength, except at the frequencies near Fabry–Pérot resonances. Near the band edge where there is very little Si absorption and propagation lengths are long, we see the most enhancement over the $10 \mu\text{m}$ area, as well as a peak at the dipole resonance of the groove. For the 150 nm thick film where the film resonance is shifted to 580 nm, we clearly observe the

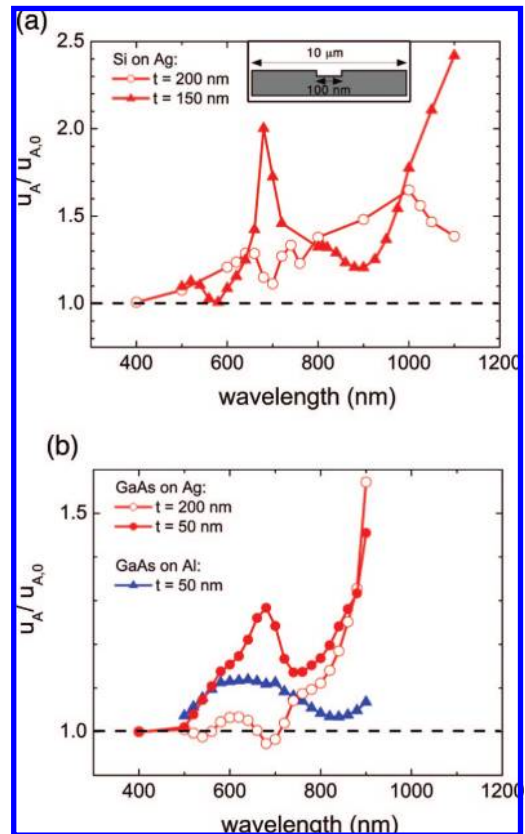


Figure 5. Absorption enhancement for a 100 nm wide by 50 nm deep groove, relative to the otherwise identical thin film with no groove: (a) Si on Ag; (b) GaAs on Ag and Al. Inset shows size of groove compared to the length of the volume considered for enhancement, $10 \mu\text{m}$. Excitation by a Gaussian beam with a $1 \mu\text{m}$ half-width.

enhancement at resonance and at the band edge, reaching an enhancement factor of 2.5 at 1100 nm.

The GaAs response is somewhat flatter than the Si response, reaching a high of 1.6 near the band edge at 880 nm. This is not surprising, since GaAs is a direct bandgap semiconductor and already a strong absorber. In this case, the semiconductor absorber layer can be made much thinner, and here we show calculations for a 50 nm thick layer on both Ag and Al. The 200 nm layer shows a relatively small enhancement, except near the band edge where absorption is low. The dips at 540 and 680 nm match the Fabry–Pérot film resonances for GaAs. For the 50 nm film on Ag, the enhancement is much greater, with a strong peak at SPP resonance and the Fabry–Pérot dip shifted to 760 nm. For the same thickness layer on Al, the spectral shape is quite different because the Fabry–Pérot resonance of the film is shifted out to longer wavelengths and has little response in the 500–800 nm region. The losses in Al are higher, however, so the overall enhancement due to semiconductor absorption is much lower. Overall, then, Ag is the preferred back contact over Al, due to the different loss ratios, and we find that, while the most absorption enhancement occurs at resonant frequencies, there is significant broadband response over a large area of the film.

Finally, in Figure 6 we consider our other incoupling design goal, angle insensitivity. Figure 6 shows the absorp-

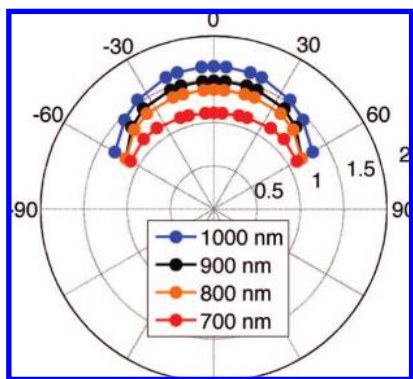


Figure 6. Absorption enhancements as a function of angle of incidence for 700–1100 nm incident light. The illumination source is a $1\ \mu\text{m}$ half-width Gaussian beam, and the enhancements are calculated over a $10\ \mu\text{m}$ area. This enhancement is relative to a control set with no groove and considers only the absorption which occurs in the Si layer.

tion enhancement ratio as a function of angle of incidence for a 100 nm wide by 50 nm deep groove in 200 nm of Si, from 0 to 60° . Since the frequencies of the Fabry–Pérot modes change with angle, the absorption enhancement is a more appropriate figure of merit than incoupling cross sections to study the intrinsic behavior of the groove. First, the absorption enhancements at all angles are ≥ 1 , indicating that there are no additional losses due to the modal incoupling at higher angles. We find that at the four frequencies monitored, in the 700–1000 nm region where there is significant power coupled into SPP modes, the enhancements are quite isotropic, confirming that single subwavelength grooves can act as broad-angle incouplers.

In conclusion, we have shown that single subwavelength scattering objects on the metallic back surface of a thin film solar cell can enhance the absorption in the semiconductor over large areas, observing up to $2.5\times$ enhancement at the longest wavelengths investigated. We find that the spectral scattering response depends on the geometric factors of the object, the thickness of the absorbing film, and the choice of materials and quantitatively show how both the incoupling cross section and semiconductor absorption can be tuned and enhanced throughout the visible spectrum. The SPP waveguide-based solar cells proposed have the potential to achieve significant absorption enhancement within small volumes of material, thereby both reducing the cost and opening the door to unusual materials with short carrier diffusion lengths.

Acknowledgment. The authors thank Albert Polman, Kylie Catchpole, and Ewold Verhagen for useful discussions. Support for this work from the Department of Energy under Grant No. DOE DE-FG02-07ER46405 and the Global Climate and Energy Project is gratefully acknowledged.

Supporting Information Available: Description of method for assessing the incoupling ability of these structures and for tracking the dissipation of power that enters the device. This material is available free of charge via the Internet at <http://pubs.acs.org>.

References

- (1) Green, M. A. *Physica E* **2002**, *14*, 65.
- (2) Keevers, M. J.; Young, T. L.; Schubert, U.; Green, M. A. 22nd European Photovoltaic Solar Energy Conference, Milan, September 2007.
- (3) Contreras, M. A.; Egaas, B.; Ramanathan, K.; Hiltner, J.; Swartzlander, A.; Hasoon, F.; Noufi, R. *Prog. Photovoltaics* **1999**, *7*, 311.
- (4) Wu, X.; Keane, J. C.; Dhare, R. G.; DeHart, C.; Duda, A.; Gessert, T. A.; Asher, S.; Levi, D. H.; Sheldon, P. Conf. Proceedings, 17th European Photovoltaic Solar Energy Conference, Munich, 22–26 October 2001, 995–1000.
- (5) Romeo, A.; Terheggen, A. *Prog. Photovoltaics* **2004**, *12*, 93.
- (6) Rim, S. B.; Zhao, S.; Scully, S. R.; McGehee, M. D.; Peumans, P. *Appl. Phys. Lett.* **2007**, *91*, 243501.
- (7) Eisele, C.; Nebel, C. E.; Stutzmann, M. *J. Appl. Phys.* **2001**, *89*, 7722.
- (8) Yablonovitch, E. *Phys. Rev. Lett.* **1987**, *58*, 2059.
- (9) Dionne, J. A.; Sweatlock, L. A.; Atwater, H. A.; Polman, A. *Phys. Rev. B* **2005**, *72*, 075405.
- (10) Raether, H. *Springer Tracts Mod. Phys.* **1988**, *111*, 1.
- (11) Ozbay, E. *Science* **2006**, *311*, 5758.
- (12) Brongersma, M. L.; Kik, P. G. *Surface Plasmon Photonics*; Springer: Dordrecht, NL.
- (13) Pacifici, D.; Lezec, H. J.; Atwater, H. A. *Nat. Photonics* **2007**, *1*, 402.
- (14) Stuart, H. R.; Hall, D. G. *Appl. Phys. Lett.* **1998**, *73*, 3815.
- (15) Pillai, S.; Catchpole, K. R.; Trupke, T.; Green, M. A. *J. Appl. Phys.* **2007**, *101*, 093105.
- (16) Nakayama, K.; Tanabe, K.; Atwater, H. A. *Appl. Phys. Lett.* **2008**, *93*, 121904.
- (17) Kretschmann, E. *Z. Phys.* **1971**, *241*, 313.
- (18) Otto, A. *Z. Phys.* **1968**, *216*, 398.
- (19) Ritchie, R. H.; Arakawa, E. T.; Cowan, J. J.; Hamm, R. N. *Phys. Rev. Lett.* **1968**, *21*, 1530.
- (20) Bethe, H. A. *Phys. Rev.* **1944**, *66*, 163.
- (21) Bouwkamp, C. J. *Philips Res. Rep.* **1950**, *5*, 321.
- (22) Chang, S.-H.; Gray, S. K.; Schatz, G. C. *Opt. Express* **2005**, *13*, 3150.
- (23) Kihm, H. W.; Lee, K. G.; Kim, D. S.; Kang, J. H.; Park, Q.-H. *Appl. Phys. Lett.* **2008**, *92*, 051115.
- (24) Leveque, G.; Martin, O. J. F.; Weiner, J. *Phys. Rev. B* **2007**, *76*, 155418.
- (25) Isaac, T. H.; Gomez Rivas, J.; Sambles, J. R.; Barnes, W. L.; Hendry, E. *Phys. Rev. B* **2008**, *77*, 113411.
- (26) Suckling, J. R.; Hibbins, A. P.; Lockyear, M. J.; Priest, T. W.; Sambles, J. R.; Lawrence, C. R. *Phys. Rev. Lett.* **2004**, *92*, 147401.
- (27) Pacifici, D.; Lezec, H. J.; Sweatlock, L. A.; Walters, R. J.; Atwater, H. A. *Opt. Express* **2008**, *16*, 9222.
- (28) Pacifici, D.; Lezec, H. J.; Atwater, H. A.; Weiner, J. *Phys. Rev. B* **2008**, *77*, 15411.
- (29) Liu, J. S. Q.; Brongersma, M. L. *Appl. Phys. Lett.* **2007**, *90*, 091116.
- (30) Baudrion, A.-L.; de Leon-Perez, F.; Mahboub, O.; Hohenhau, A.; Ditzbacher, H.; Garcia-Vidal, F. J.; Dintinger, J.; Ebbesen, T. W.; Martin-Moreno, L.; Krenn, J. R. *Opt. Express* **2008**, *16*, 3420.
- (31) Heavens, O. S. *Optical Properties of Thin Solid Films*; Dover Publications: New York, 1991.
- (32) Kurokawa, Y.; Miyazaki, H. T. *Phys. Rev. B* **2007**, *75*, 035411.
- (33) Bohren, C. F.; Huffman, D. R. *Absorption and Scattering of Light by Small Particles*; John Wiley & Sons: New York, 1983.
- (34) Yaghjian, A. D. *IEEE Trans. Antennas Propag.* **2007**, *55*, 1495.

NL8022548